ARTICLE

Numerical Investigations on Effects of Physical Parameters on Single Bubble Generation from Capillary Needles in Newtonian Liquids

Meng Jia and Mingjun Pang[*]

School of Mechanical Engineering and Rail Transit, Changzhou University, Changzhou, 213164, China

*Corresponding Author: Mingjun Pang. Email: pangmj@cczu.edu.cn

ABSTRACT

The interphase mass, heat transfer efficiency, and flow resistance are strongly dependent on bubble size in gas-liquid two-phase systems, so it is very important for engineering applications to effectively control bubble size. In this paper, the formation, growth, and detachment of single bubbles in Newtonian liquids based on capillary needles were studied in detail using a volume of fluid method. The authors investigated the effects of gas injection velocity, gravitational level, surface tension coefficient, needle radius, and liquid−phase properties (liquid viscosity and density) on the process of bubble generation, and the effects of the above factors on bubble shape, detachment diameter, and time were analyzed. The results show that an increase in gas injection rate, liquid-phase viscosity, needle radius, and surface tension coefficient can lead to an increase in bubble detachment diameter; however, an increase in liquid-phase density and gravitational level can lead to a decrease in bubble detachment diameter. It is found that the effect of the liquid−phase viscosity on bubble detachment diameter and time is slight, but the effect of gravitational level on detachment diameter and time is significant. Among all the forces, buoyancy, surface tension, and pressure are the most important ones that control the generation of bubbles.

KEYWORDS

Bubble generation; detachment diameter; capillary needles; VOF

Nomenclature

A	Gravity level
C	Drag coefficient
D	Bubble detachment diameter
f	Phase function
F	Force
g	Acceleration of gravity
k_s	Curvature of bubble interface
$\hat{\boldsymbol{n}}$	The unit normal vector
Q	Gas flow
R	Radius of bubbles
r	Needle radius

Re	Reynolds number
t∗	Normalized time
t	Bubble detachment time
u	Velocity vector
v	Gas injection velocity
V	Instantaneous volume of bubbles
Y	Axial centroid position of bubbles
∇	Hamiltonian operator

Greek Symbols

δ	Dirac distribution function
μ	Viscosity
ρ	Density
σ	Surface tension coefficient

Subscripts

AM	Added mass force
b	Bubble
B	Buoyancy force
CM	Centroid position
D	Viscous drag
det	Detachment time or diameter
g	Gas phase
l	Liquid phase
M	Gas momentum force
o	Orifice diameter
P	Pressure
S	Surface tension

1 Introduction

Gas−liquid two−phase systems can be frequently seen in industrial and medical processes such as aeration, fermentation, metallurgy, water treatment, blood oxygenators, bubbling towers, fluidized beds, and jet reactors [1–3]. Bubble size determines the rising velocity and residence time of a bubble in liquid and its wake flow. These aspects can further affect the performance of two−phase systems, such as their heat and mass transfer efficiencies and mixing and drag behaviors. Therefore, it is very significant to investigate deeply various physical parameters affecting the generation of bubbles to understand the physical mechanism of multiphase flows concerning interfacial phenomena and improve the performance of gas−liquid two−phase systems. To fully understand the influence of various factors on the formation of bubbles in Newtonian fluids, many investigations have been carried out till now. Kulkarni et al. [4] carried out a detailed review of early studies. Wang et al. [5] reviewed the regulation of bubble size in flotation. Suja et al. [6] provided a comprehensive discussion of the various single bubble/drop platforms and the associated experimental measurement protocols. Gardner et al. [7] reviewed bubble formation in magma. Recent typical investigations on bubble generation are reviewed as follows.

First, a number of numerical studies on the formation and detachment characteristics of bubbles have been conducted. Martín et al. [8] performed numerical calculations of shapes and detachment times of bubbles generated from a sieve plate, and a mathematical model describing the formation, breakage, and rising of a gas bubble generated in a submerged orifice was proposed. Quan et al. [9] numerically investigated the pinch-off of a gas bubble from a tiny nozzle immersed vertically in another quiescent viscous fluid due to buoyancy. Chakraborty et al. [10] numerically analyzed the dynamic problem of bubble formation from a submerged orifice in an immiscible Newtonian liquid under the condition of constant gas inflow. Ma et al. [11] numerically investigated the single bubble formation and dynamics in bubble columns with the volume of fluid (VOF) model. di Bari et al. [12] numerically simulated the growth of adiabatic gas bubbles from a submerged orifice with the finite volume method. Albadawi et al. [13,14] numerically investigated bubble growth and detachment at low Capillary and Bond numbers using Volume of Fluid and Level Set methods. Georgoulas et al. [15] numerically investigated the effect of fluid properties and gravity levels on quasi-static bubble growth and detachment from submerged orifices in isothermal liquid pools using VOF. Simmons et al. [16] simulated the formation of a single bubble from an orifice in a solid surface submerged in an incompressible and viscous Newtonian liquid. Hecht et al. [17] numerically studied the influence of wettability on the formation of a single air bubble at a submerged orifice. Ali et al. [18] performed numerical modeling for the characterization of CO_2 bubble formation through submerged orifice in ionic liquids. Oshaghi et al. [19] performed a numerical investigation of bubble formation and detachment in shear-thinning liquids at low capillary and Bond numbers. Boubendir et al. [20] numerically investigated the surface tension role in bubble growth and detachment in a micro-tube. Smith et al. [21] numerically studied the role of surface tension on the growth of bubbles by rectified diffusion.

Second, many experimental studies under different conditions have also been carried out. Burton et al. [22] used a 100,000 frame-per-second video to analyze the pinch-off of nitrogen gas bubbles in fluids with a wide range of viscosity. Duhar et al. [23] experimentally investigated the quasistatic injection of air bubbles at the wall in a viscous shear flow by high-speed video pictures and image processing. Taghi Esfidani et al. [24] presented both theoretical and experimental studies on the size of a growing bubble in power-law non-Newtonian liquids. Hanafizadeh et al. [25] investigated experimentally the effect of orifice shape on the mechanism of bubble formation in gas–liquid two–phase flow with three different orifice geometries with the same cross-sectional areas. Sun et al. [26] investigated experimentally the effects of liquid temperature, aerosol, and gas–phase composition on bubble formation characteristics. Mohseni et al. [27] experimentally investigated bubble generation based on micro-orifices and needles with very fine orifice diameters in the range from 37 to 225 µm. Muilwijk et al. [28] performed an experimental investigation on the bubble formation from needles with and without liquid co-flow. Sattari et al. [29] conducted an experimental investigation of bubble formation on submerged micrometer−sized nozzles in polymer solutions. Mohseni et al. [30] experimentally studied the mechanism of bubble formation and detachment at orifices smaller than 1 mm in diameter. Li et al. [31] numerically and experimentally investigated the production of bubbles in flotation equipment using the jet microbubble generator. Muilwijk et al. [32] experimentally studied the formation of bubbles in the presence and absence of liquid co−flow with dual−tip optical fiber probes. They also performed experimental investigations of asymmetric bubble column configurations using bubble image velocimetry and dual−tip optical fiber probes [33]. Reuter et al. [34] studied the dynamics leading to the needle jet formation with high-speed imaging at five million frames per second under femtosecond illumination. Garivalis et al. [35] experimentally investigated the nucleation and growth of single bubbles at a heated surface immersed in an electric field at the microgravity

level. Sheng et al. [36] experimentally investigated the mechanism and modeling of Taylor bubble generation in highly viscous fluids in a T−junction via the vertical squeezing route. Rajesh et al. [37] experimentally studied the pinch−off of bubbles in polymer solutions of different concentrations, showing that the bubble neck is tightly related to liquid−phase viscosity. Tanaka et al. [38] used the direct observation technique of quartz glass to study the process of bubble formation in the molten pool during laser cladding. Shi et al. [39] carried out an experiment on the effect of gas injection rate on bubble generation characteristics during coal floatation. Sarkar et al. [40] experimentally studied the dynamics of bubble formation (such as bubble detachment diameter and time) at the tip of top−submerged nozzles immersed in a quiescent liquid. Qiu et al. [41] quantitatively investigated how electrolyte solutions impact bubble departure diameters due to their physical properties and the electrode surface exposed to the electrochemical reactions based on experimental observation.

Again, some researchers performed the theoretical prediction of bubble formation. A force balance model for calculating bubble detachment diameter during flow boiling is derived by Manthey et al. [42]. It was concluded that the magnitude of the inclination angle is not important for the calculation of bubble detachment diameter. In short, although some studies on bubble generation have been conducted, accurate prediction models and perfect mechanism explanations of bubble formation are further needed to investigate and develop. Presently, most of the conclusions are achieved under specific conditions, and some results are contradictory, as pointed out by Jamialahmadi et al. [43]. To deeply understand the physical phenomenon of bubble formation, this paper investigates in detail the effects of physical parameters such as liquid density and viscosity, gas injection rate, gravitational level, surface tension coefficient, and needle radius on bubble shape and detachment characteristics.

2 Physical Problems and Governing Equations

2.1 Geometric Model

To save computational costs, the computational region is simplified to a two−dimensional axisymmetric model, as shown in Fig. 1, where a single bubble is generated from the top of a capillary needle with a radius of r_o. To eliminate the influence of the wall effect on bubble generation and to ensure the full growth of bubbles in the vertical direction, the size of L and H are set to 10 r_o and 20 r_o. To simulate the generation of a single bubble, the following assumptions are presented: (1) the gas flow rate in a capillary needle is low, and all the gas is used to generate bubbles; (2) the generation of bubbles occurs under a quasi−static condition; (3) the compressibility of gas is ignored; (4) the generated bubble is spherical and can be seen as a circle in the two−dimensional axisymmetric model.
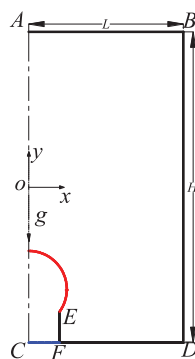

Figure 1: Geometric model

2.2 Design of Computational Cases

The present investigations show that bubble generation is mainly influenced by gas and liquid thermophysical parameters, gas injection velocity, and needle radius. Therefore, the effects of parameters such as liquid density (ρ_l), liquid viscosity (μ_l), surface tension coefficient (σ), gas injection velocity (v_g), needle radius (r_o), and gravitational level (a) are investigated here. To investigate the quantitative effects of the above parameters on bubble detachment characteristics (such as detachment time and volume), a set of data for these six parameters is selected ($\rho_l = 1000$ kg/m³, $\rho_g = 1.225$ kg/m³, $\sigma = 0.065$ N/m, $\mu_l = 0.001$ Pa·s, $\mu_g = 1.7894 \times 10^{-5}$ Pa·s, and $a = 9.81$ m/s²) as basic ones. Then, the other parameters remain constant, and changing one or two ones is to study their effects on bubble detachment characteristics. For example, the effect of liquid density ($\rho_l = 500$–2500 kg/m³) on bubble detachment characteristics is studied at $r_o = 0.1$ and 1.0 mm at $v_g = 0.1$ and 1.0 m/s, respectively. All computational conditions are shown in Table 1.

Table 1: Computational parameters

Fixed parameters	Variable parameters	
$\rho_g = 1.225$ kg/m³, $\sigma = 0.065$ N/m, $\mu_l =$ 0.001 Pa·s, $\mu_g = 1.7894 \times 10^{-5}$ Pa·s, $g =$ 9.81 m/s²	$r_o = 0.5$ and 1.0 mm $v_g = 0.1$ and 1.0 m/s	$\rho_l = 2500, 2000, 1500, 1000,$ 750, 500 kg/m³
$\rho_l = 1000$ kg/m³, $\rho_g = 1.225$ kg/m³, $\sigma =$ 0.065 N/m, $\mu_g = 1.7894 \times 10^{-5}$ Pa·s, $g =$ 9.81 m/s²	$r_o = 0.3$ and 1.0 mm $v_g = 0.2$ and 0.1 m/s	$\mu_l = 0.001, 0.01, 0.08, 0.1,$ 0.2, 0.3, 0.4, 0.5 Pa·s
$\rho_l = 1000$ kg/m³, $\rho_g = 1.225$ kg/m³, $\mu_l =$ 0.001 Pa·s, $\mu_g = 1.7894 \times 10^{-5}$ Pa·s, $g =$ 9.81 m/s²	$r_o = 0.3$ and 1.0 mm $v_g = 0.1$ and 2 m/s	$\sigma = 0.072, 0.065, 0.05, 0.04,$ 0.03, 0.02, 0.01 N/m
$\rho_l = 1000$ kg/m³, $\rho_g = 1.225$ kg/m³, $\sigma =$ 0.065 N/m, $\mu_l = 0.001$ Pa·s, $\mu_g = 1.7894$ $\times 10^{-5}$ Pa·s, $g = 9.81$ m/s²ᵃᵗ	$r_o = 0.3, 0.5, 0.8,$ 1.0, 1.5 mm	$v_g = 0.05, 0.1, 0.2, 0.4, 0.6,$ 0.8, 1.0, 1.5, 2.0, 2.5, 3.0 m/s
$\rho_l = 1000$ kg/m³, $\rho_g = 1.225$ kg/m³, $\sigma =$ 0.065 N/m, $\mu_l = 0.001$ Pa·s, $\mu_g = 1.7894$ $\times 10^{-5}$ Pa·s	$r_o = 1$ mm and $v_g = 0.1$ m/s	$a = 10.99, 9.81, 8.83, 7.0,$ 3.71 m/s²

2.3 Governing Equations

Presently, it is assumed that the flow is adiabatic and axisymmetric, the injection velocity of gas is uniform, and a two−phase flow is formed at the needle top. Both fluids are considered to be mutually impermeable and incompressible Newtonian ones. The continuity and momentum equations are presented by Eqs. (1) and (2).

$$\nabla \cdot \boldsymbol{u} = 0 \tag{1}$$

$$\frac{\partial \rho \boldsymbol{u}}{\partial t} + \nabla \cdot (\rho \boldsymbol{u}\boldsymbol{u}) = -\nabla p + \nabla \cdot \mu \left(\nabla \boldsymbol{u} + \nabla \boldsymbol{u}^T \right) + \rho \boldsymbol{g} + \boldsymbol{F}_s \tag{2}$$

where $\boldsymbol{u}$ is the velocity vector, m/s; p is the pressure, Pa; $\boldsymbol{g}$ is the acceleration of gravity, m/s²; ρ is the average density of the fluid, kg/m³; μ is the average viscosity of the fluid, Pa·s; t is the time, s; and ∇

is the Hamiltonian operator. $\boldsymbol{F}_S$ is the volume force due to surface tension, N; and it is calculated by Eq. (3).

$$\boldsymbol{F}_s = \sigma k_s \delta \hat{\boldsymbol{n}} \tag{3}$$

where σ is the surface tension coefficient, N/m; and δ is the Dirac distribution function. k_s is the curvature of the bubble interface, and $\hat{\boldsymbol{n}}$ is the unit normal vector of the outward direction of the interface, which are calculated by Eq. (4), respectively.

$$k_s = -\nabla \cdot \hat{\boldsymbol{n}} \left(\hat{\boldsymbol{n}} = \frac{\boldsymbol{n}}{|\boldsymbol{n}|} \right) \tag{4}$$

The average density and viscosity of fluids are calculated by Eqs. (5) and (6).

$$\rho = \rho_l (f) + \rho_g (1 - f) \tag{5}$$

$$\mu = \mu_l (f) + \mu_g (1 - f) \tag{6}$$

In Eqs. (5) and (6), f denotes the phase function, which is defined by Eq. (7).

$$f = \begin{cases} 0 & \text{Bubble} \\ 0 < f < 1 & \text{Interface} \\ 1 & \text{Liquid} \end{cases} \tag{7}$$

2.4 Interface Capture Method

The VOF method is used to track the volume of fluids in each grid rather than the motion of fluid particles, and thus it has the advantages of simple implementation, low computational complexity, and high accuracy compared with other methods. For the VOF method, two kinds of fluids share a set of momentum equations, and the volume fraction of each fluid in each cell is tracked in the whole domain. The VOF method utilizes the volume ratio of fluids in each grid (i.e., f) to achieve the goal based on the fact that two or more fluids are not interpenetrating [11]. The transport equation of f is presented by Eq. (8).

$$\frac{\partial f}{\partial t} + \boldsymbol{u} \cdot \nabla f = 0 \tag{8}$$

2.5 Interface Reconstruction

Since f is not explicitly related to a specific front grid for the VOF method, an algorithm is needed to reconstruct the bubble interface. There are several methods to solve the volume functions of fluids, such as the donor−acceptor method, the flux line−segment model for advection and interface reconstruction method, the simple line interface calculation method, and the piecewise linear interface calculation method (PLIC) [44]. The PLIC method takes into account the transfer of fluids between adjacent interfaces in detail, and thus the reconstruction results are relatively accurate. Therefore, the PLIC method is applied to interface reconstruction here. For the PLIC method, the interface in each cell is approximated by a straight line defined by $\boldsymbol{n} \cdot \boldsymbol{x} + C = 0$, where $\boldsymbol{n}$ and $\boldsymbol{x}$ are the outward unit vector normal to the interface and the position vector of a generic point on the line, respectively, and C is a constant [44].

2.6 Numerical Methods

For the present calculation, the velocity inlet is applied to the wall of CF, the no−slip wall is applied to the ones of EF, DF, and BD, the pressure outlet is applied to the wall of AB, and the

line of AC is the symmetrical axis. Compared with the unstructured grid, the structured grid can be quickly generated, it is easy to fit the boundary of the calculation region, and it has the advantages of good grid quality, high calculation accuracy, and easy calculation convergence. Therefore, the structured grid is applied to the present computation. The coupling between pressure and velocity fields is achieved by the SIMPLE algorithm. The pressure and momentum terms are discretized using staggered pressure PRESTO and second−order windward schemes, respectively. Time steps are variable, the global Courant number is 0.25, and correspondingly the minimum time step is 10^{-5} s. Before the calculation starts, the initialization is performed so that the calculation domain is filled with stationary liquid, and the needle is filled with gas. Then, the two−phase flow calculation starts. The present computations are performed using ANSYS 18.0.

3 Results and Discussion

3.1 Validation of Results

To analyze the process of bubble formation under different conditions, the normalized time t^* is defined as follows:

$$t^* = t/t_{det} \tag{9}$$

where t and t_{det} are any point in time and the detachment time of bubbles during the formation process, respectively. Four dimensionless times of $t^* = 0.2$, $t^* = 0.5$ and 0.7, and $t^* = 1$ are chosen to represent the early, middle, and late stages of bubble generation.

3.1.1 Validation on Results Independent of Grid Size

To check if the calculation results are independent of grid size, for the computational conditions of $r_o = 1 \times 10^{-3}$ m, $v_g = 0.1$ m/s, and the basic parameters, five grid systems are designed. They are Grid 1, Grid 2, Grid 3, Grid 4, and Grid 5, and the corresponding sizes are 0.1, 0.05, 0.033, 0.025, and 0.017 mm, respectively. The calculation results are shown in Fig. 2 and Table 2. It can be seen from Fig. 2 and Table 2 that the bubble interface becomes thinner and thinner, and the separation time of bubbles remains constant with a decrease in grid size. There is a deviation in the calculation results of Grids 1 and 2, while the results of Grids 3, 4, and 5 are basically the same. To reduce the calculation cost and obtain the accurate results, the maximum grid size is less than 0.033 mm for subsequent computations.
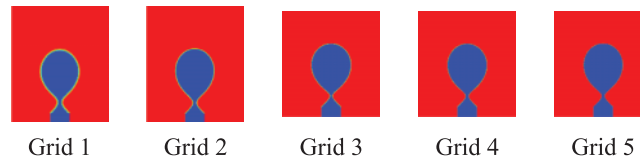

Grid 1   Grid 2   Grid 3   Grid 4   Grid 5

Figure 2: Bubble shapes at separation time for different grid sizes

3.1.2 Validation on Results Independent of Grid Size

To verify the accuracy of computational results, the experimental and numerical cases of Quan et al. [9] are selected as the validation ones. The definite parameters are $r_o = 1.35 \times 10^{-3}$ m, $\rho_l = 1000$ kg/m³, $\rho_g = 1.005$ kg/m³, $\sigma = 0.065$ N/m, $\mu_l = 0.001$ Pa·s, $\mu_g = 1.42 \times 10^{-5}$ Pa·s, $g = 9.81$ m/s², and $v_g = 0.005$ m/s. The comparison of results is shown in Fig. 3. It can be seen from Fig. 3 that the present calculation result is basically consistent with that of reference [9]. Because the gas

injection velocity is not specified in the reference, the numerical results are slightly different from those in the reference. This shows that the present computational method is credible.

Table 2: Separation time of bubbles for different grid sizes

	Grid size (mm)	t_{det} (s)	Error (%)
Grid 1	0.100	0.118	4.06
Grid 2	0.050	0.123	0
Grid 3	0.033	0.123	0
Grid 4	0.025	0.123	0
Grid 5	0.017	0.123	0
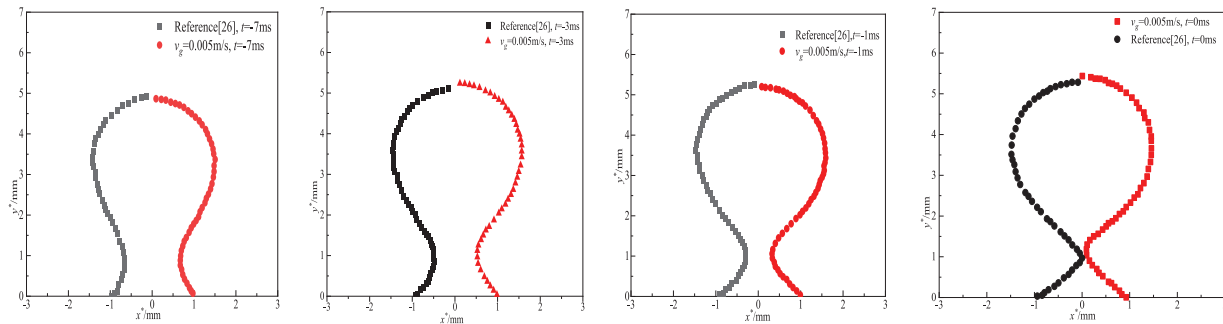
Figure 3: Bubble formation process (The left side is the results of reference [9])

3.2 Analysis of Bubble Generation Process Shape

Fig. 4 shows the formation process of a bubble for $r_o = 1 \times 10^{-3}$ m, $v_g = 0.1$ m/s, and the basic parameters. In Fig. 4, the red region represents the liquid phase, and the blue region represents the gas phase. It can be seen that the bubble volume increases rapidly with time. At the middle stage of bubble generation (i.e., $t^* = 0.5$–0.7), the bubble is axially elongated due to buoyancy force and pressure. At the late stage of bubble generation ($t^* = 1$), a neck appears at the bubble bottom. The diameter of the bubble neck decreases rapidly, leading to the separation of the bubble. The results of other cases will be compared with the present one to illustrate the influence of each factor on the bubble generation process.
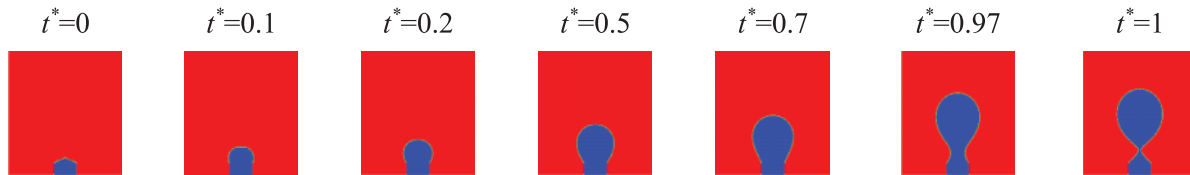

Figure 4: Variation of bubble shape with time for $r_o = 1 \times 10^{-3}$ m, $v_g = 0.1$ m/s and the basic parameters

3.2.1 Gas Injection Velocity

Fig. 5 shows the effect of v_g on bubble shape during the formation process for $r_o = 1 \times 10^{-3}$ m and the basic parameters. It can be seen from Fig. 5 that with an increase in v_g, the bubble shape deviates from the spherical one. The present phenomenon is consistent with that of reference [10]. This indicates that the assumption of spherical bubbles is not always correct. In addition, the bubble volume increases rapidly as v_g increases at the same dimensionless time. The present results are similar to those of reference [4]. In the early stage of bubble generation ($t^* = 0.2$), with an increase in v_g, the lateral size of bubbles increases and exceeds the needle diameter. In the middle stage of bubble generation ($t^* = 0.5$–0.7), with an increase in v_g, the bubble bottom gradually becomes fan−shaped, the bubble top deviates from the hemisphere first and then it gradually returns to the hemisphere again, and the bubble gradually rises upwards. The larger the v_g is, the greater the degree of bubble axial stretching is. At the later stage of bubble generation ($t^* = 1$), the bubble neck appears, and it is obvious that the greater v_g is, the greater the axial height of bubbles is.
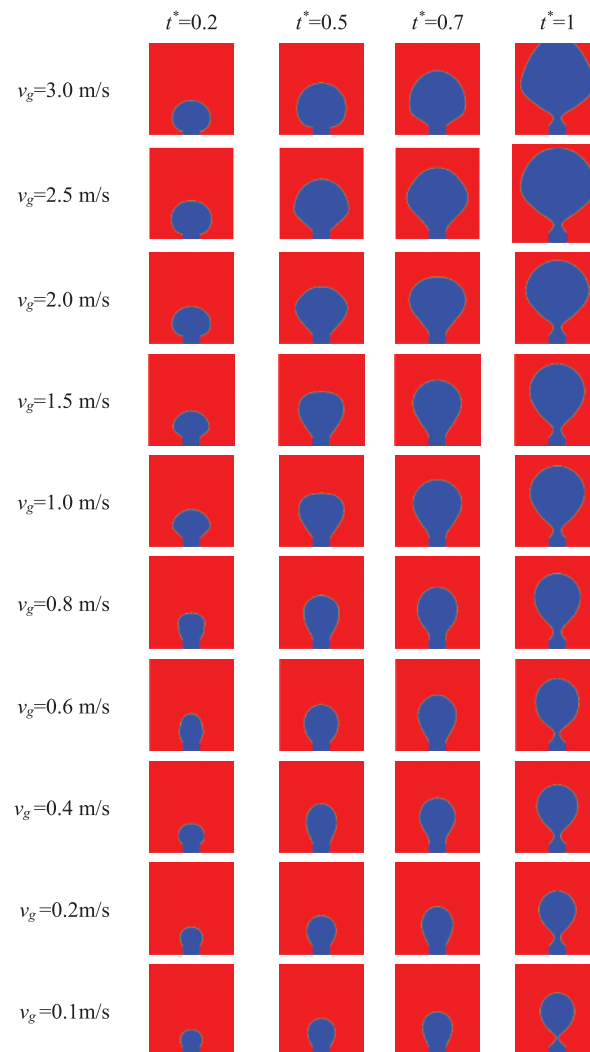

Figure 5: Variation of bubble shape with time for different v_g ($r_o = 1 \times 10^{-3}$ m and the basic parameters)

3.2.2 Gravity Level

Fig. 6 shows the effect of a on bubble shape during the formation process for $r_o = 1 \times 10^{-3}$ m, $v_g = 0.1$ m/s, and the basic parameters. It can be seen from Fig. 6 that as a increases, bubble volume decreases at the same dimensionless time. This means that the greater a is, the shorter the time required for bubble detachment. Therefore, the bubble volume is smaller when other physical parameters are the same. It is obvious that the magnitude of a has an important effect on bubble generation, as pointed out by Georgoulas et al. [15].
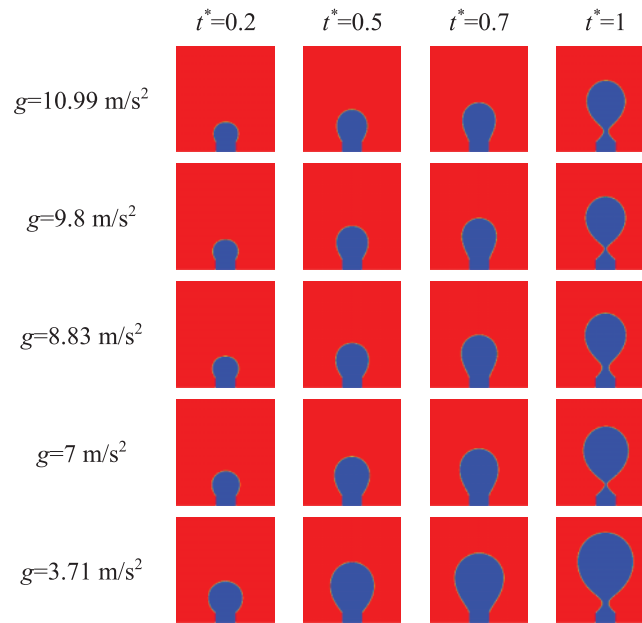

Figure 6: Variation of bubble shape with time under different a ($r_o = 1 \times 10^{-3}$ m, $v_g = 0.1$ m/s and the basic parameters)

3.2.3 Surface Tension Coefficient

Fig. 7 shows the effect of σ on bubble shape during the formation process for $r_o = 1 \times 10^{-3}$ m, $v_g = 0.1$ m/s, and the basic parameters. It can be seen from Fig. 7 that the smaller σ is, the greater the deformation of the bubble interface is, and the smaller the bubble volume at the same time is. This is because the force of the bubble attachment to the needle increases as σ (i.e., the surface tension) increases. Bubble detachment becomes difficult. Therefore, as σ increases, the bubble needs a larger volume to generate great buoyancy to promote it to detach from the needle.

3.2.4 Liquid Viscosity

Fig. 8 shows the effect of μ_l on bubble shape during the formation process for $r_o = 1 \times 10^{-3}$ m, $v_g = 0.1$ m/s, and the basic parameters. As shown in Fig. 8, in the low viscosity range (0.001−0.01 Pa·s), the bubble volume at different moments is almost the same, and the bubble size is almost independent of μ_l. However, in the higher viscosity range (0.08−0.5 Pa·s), the bubble volume at different moments increases with an increase in μ_l. When μ_l is great, the bubble is subjected to a great viscous drag. The buoyancy force must be great enough to cause the bubble to detach from the needle. Therefore, the bubble volume becomes large in highly viscous liquids.
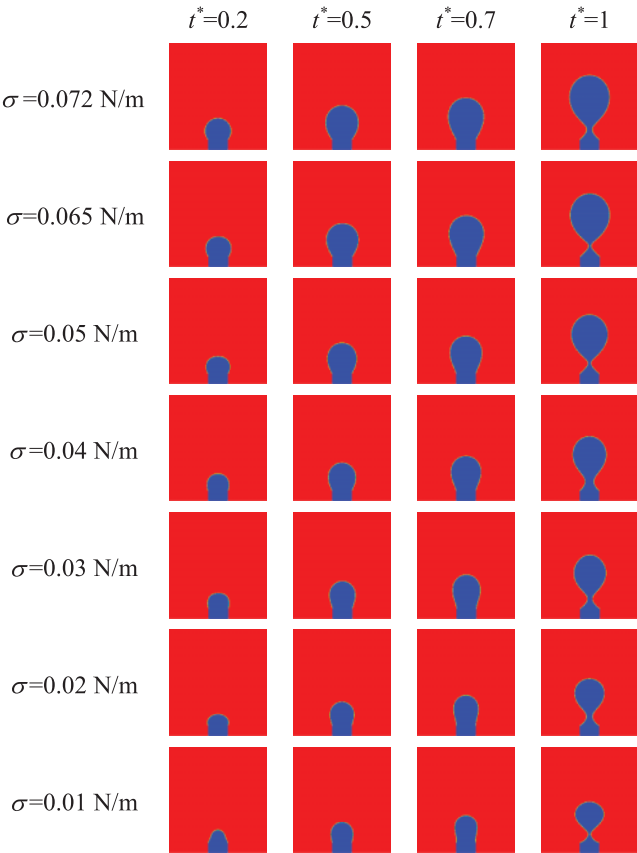
Figure 7: Variation of bubble shape with time for different σ ($r_o = 1 \times 10^{-3}$ m, $v_g = 0.1$ m/s and the basic parameters)
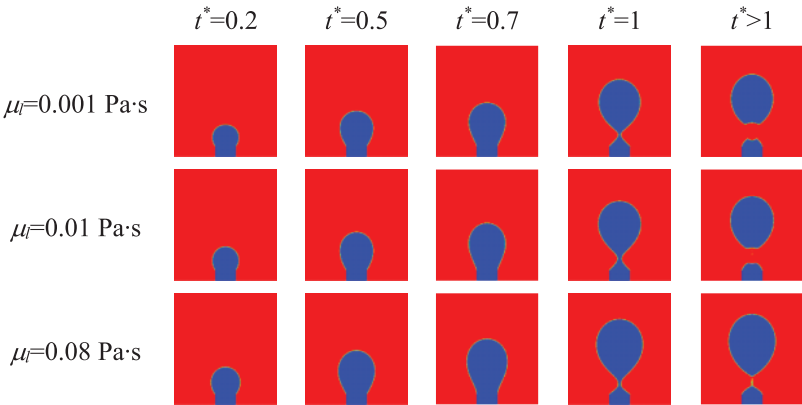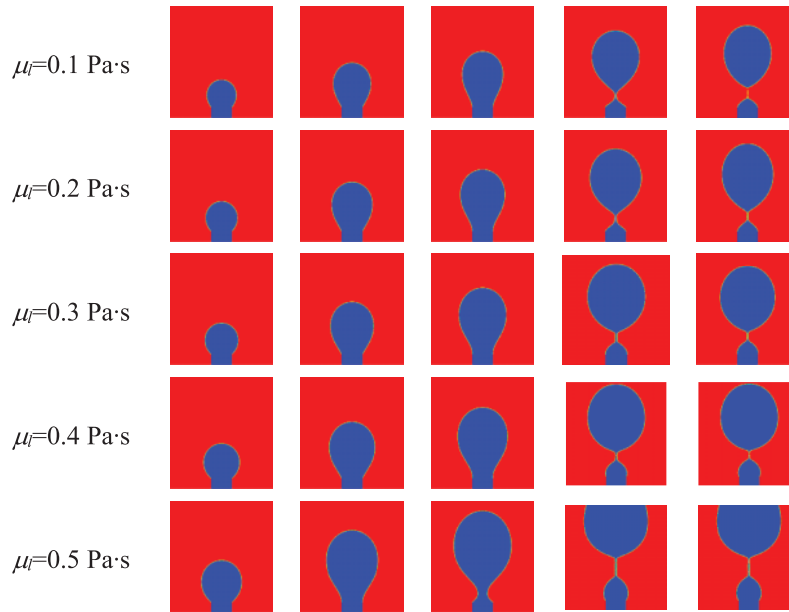

Figure 8: (Continued)

Figure 8: Variation of bubble shape with time for different μ_l ($r_o = 1 \times 10^{-3}$ m, $v_g = 0.1$ m/s and the basic parameters)

Burton et al. [22] classified the shape of bubble necks during the separation process into three types according to the magnitude of μ_l: (1) $\mu_l > 0.1$ Pa·s, the bubble neck is cylindrical in shape with a constant parabolic axial curvature, and its profile is not self−similar. The neck diameter shrinks continuously until the bubble separates into two pieces with sharp ends. The results for $\mu_l = 0.2$, 0.3, 0.4, and 0.5 Pa·s belong to this type. (2) At $0.01 < \mu_l \leq 0.1$ Pa·s, the neck radius no longer decreases linearly with time, and the axial curvature of the neck parabola is no longer a constant. The thin line formed by the parabolic stretching continues for a very long time and breaks suddenly into dozens of small satellite bubbles. The results for $\mu_l = 0.08$ and 0.1 Pa·s belong to this type. (3) At $\mu_l \leq 0.01$ Pa·s, the bubble neck becomes hyperbolic instead of parabolic in shape. The neck radius does not smoothly decrease to zero or a finite constant, and it suddenly breaks at the neck radius of 25 μm. The results for $\mu_l = 0.001$ and 0.01 Pa·s belong to this type.

3.2.5 Liquid Density

The effect of ρ_l on bubble shape during the formation process for $r_o = 1 \times 10^{-3}$ m, $v_g = 0.1$ m/s, and the basic parameters is shown in Fig. 9. It can be seen from Fig. 9 that a decrease in ρ_l also leads to an increase in the bubble volume at the same time. Namely, it leads to an increase in bubble separation volume. A decrease in ρ_l can lead to a decrease in the density difference between two phases. Therefore, a bubble must reach a large volume so that buoyancy becomes large enough to separate it from the needle rim, as reported in reference [15].
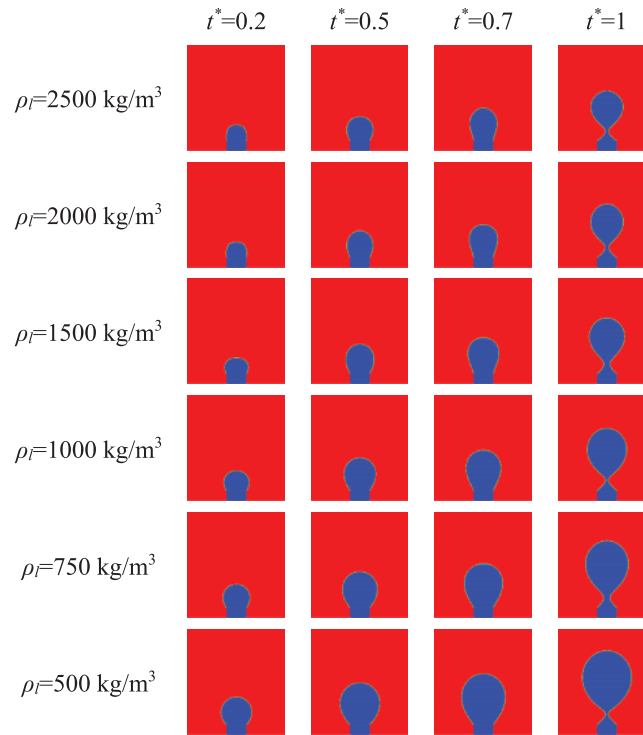
Figure 9: Variation of bubble shape with time for different ρ_l ($r_o = 1 \times 10^{-3}$ m, $v_g = 0.1$ m/s and the basic parameters)

3.2.6 Needle Radius

Fig. 10 shows the effect of r_o on bubble shape during the formation process for $v_g = 0.1$ m/s and the basic parameters. It can be seen from Fig. 10 that the shape of bubbles from a small needle is closer to the spherical one. With an increase in r_o, the bubble volume becomes large at the same time. During the early stage, the buoyancy force is very small. There is an approximate balance between surface tension and pressure force. The gas moment force is tiny during the whole process of bubble formation. At this time, the viscous drag and the added mass force are relatively important, so the bubble remains attached to the orifice until it has grown to a great size when the buoyancy force becomes very important, and the bubble is driven away from the orifice in the vertical direction. An increase in bubble growth time allows much more gas to flow into the bubble, thereby causing an increase in bubble size. Therefore, the needle with a large r_o can generate a large bubble, as pointed out by reference [45].

3.3 Analyses of Bubble Detachment Diameter and Time

It is very helpful for quantitatively understanding the influence of each factor on bubble generation to analyze bubble detachment diameter and time. The effects of v_g, r_o, a, σ, μ_l, and ρ_l on bubble detachment diameter and time are analyzed below in detail. Bubble detachment time (t_{det}) is defined as the time required from the start of gas entering into the needle to the formation and detachment of the first bubble from a needle. When v_g is a constant, the gas injection rate can be written as $Q_g = \pi r_o^2 \cdot v_g$ according to reference [46]. It is assumed that a bubble is spherical, and the bubble detachment volume

is approximately equal to $V_{det} = t_{det} \cdot Q_g$. Therefore, the bubble detachment diameter is approximated as $D_{det} = 2 \left(3V_{det}/4\pi \right)^{1/3}$.
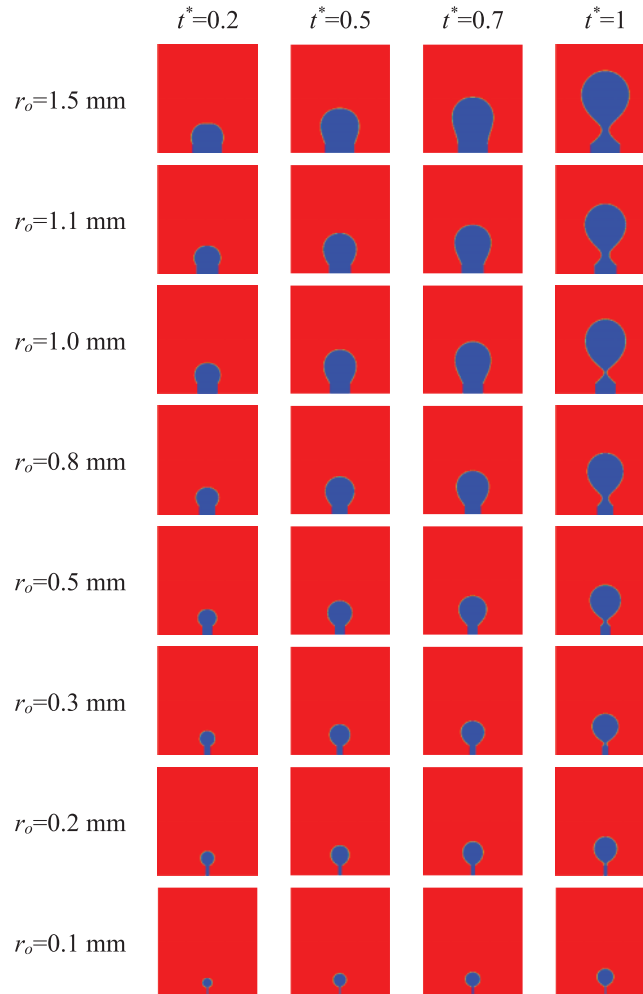

Figure 10: Variation of bubble shape with time for different r_o ($v_g = 0.1$ m/s and the basic parameters)

3.3.1 Air Inlet Velocity and Needle Radius

As shown in Figs. 5 and 10, v_g and r_o have a significant effect on the bubble generation process. Fig. 11 shows the effect of v_g and r_o on D_{det} and t_{det}. It can be seen from Fig. 11 that D_{det} increases with an increase in v_g and r_o. For a constant v_g, D_{det} increases with an increase in r_o. For a small v_g, D_{det} does not increase much with an increase in r_o; however, for a great v_g, D_{det} increases greatly with an increase in r_o. It is obvious that the increase of D_{det} with an increase in r_o is not the same for different v_g. In the case of a constant r_o, D_{det} is small for a small r_o, the increase of D_{det} with an increase in v_g is not obvious; however, the reverse applies for a great r_o. It can be seen that the effects of v_g and r_o on D_{det} are very complex.
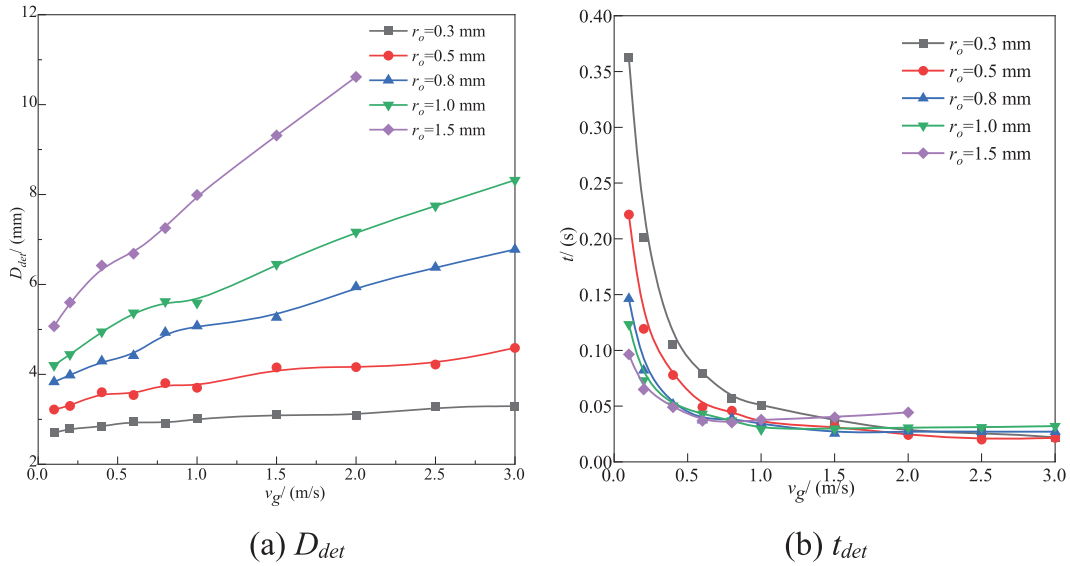
(a) D_{det} (b) t_{det}

Figure 11: Variation of D_{det} and t_{det} with v_g for different r_o

In fact, an increase in v_g and r_o leads to an increase in the flow rate of gas at the inlet. This means that the volume of gas entering the bubble increases at the same time, and thus D_{det} increases. This is similar to the results of reference [43], but it is slightly different from the results of Oguz et al. [47]. Oguz et al. [47] pointed out that when the flow rate of gas injection is less than a threshold value, the effect of gas momentum is much smaller than that of surface tension and viscous forces, and the buoyancy force is mainly balanced by surface tension and viscous forces. Thus, D_{det} is independent of the gas flow rate. However, for the present study, when r_o (such as 0.3 mm) is small, and v_g is less than the critical value (according to $Q_{cr} = \pi \, (16/3g^2)^{1/6} \, (\sigma r_o/\rho_l)^{5/6}$ [47], $v_{g,cr} = 2.6$ m/s), D_{det} is almost not affected by v_g. When r_o (such as 1 mm) is large, and v_g is less than the critical value ($v_{g,cr} = 0.6$ m/s), D_{det} increases slightly with an increase in v_g. When v_g is greater than the critical value, D_{det} increases significantly with an increase in v_g. This is because D_{det} is strongly dependent on r_o, in addition to v_g.

In addition, when r_o is a constant, the larger v_g is, the faster bubble generation velosity is, and the shorter t_{det} is. When v_g is a constant, at a low v_g, the larger r_o is, the shorter t_{det} is. For a small r_o, t_{det} decreases substantially with an increase in v_g. However, for a large r_o, t_{det} decreases slightly with an increase in v_g. This is because when r_o increases, the amount of gas entering the bubble increases at the same time. This leads to a rapid increase in buoyancy force. Therefore, the bubble detachment becomes quick. Fig. 11 also shows that when v_g is low ($v_g < 1.0$ m/s), t_{det} decreases substantially with an increase in v_g; however, when v_g is large, an increase in v_g has almost no effect on t_{det}. This phenomenon is consistent with the results of Bhunia et al. [46] under low gravity and microgravity conditions.

3.3.2 Gravity Level

Fig. 12 shows the effect of a on D_{det} and t_{det} for $r_o = 1 \times 10^{-3}$ m, $v_g = 0.1$ m/s, and the basic parameters. As shown in Fig. 12, the trends of D_{det} and t_{det} varying with a are basically similar. The higher a is, the smaller D_{det} and t_{det} are. The relationship between D_{det} (t_{det}) and a is not exactly linear, and a decrease in D_{det} (t_{det}) with an increase in a is various. This is similar to the conclusion of reference [12].
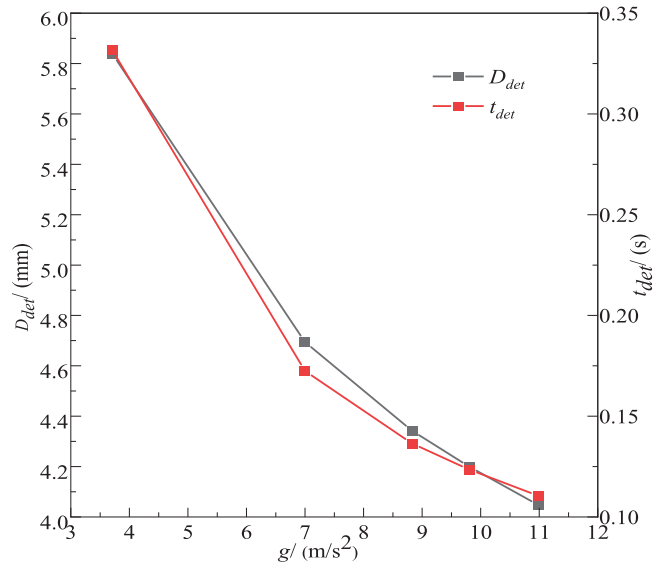
Figure 12: Effect of a on D_{det} and t_{det}

3.3.3 Surface Tension Coefficient

Fig. 13 shows the effect of σ on D_{det} and t_{det} for the fixed r_o and v_g, and the basic parameters. It can be seen from Fig. 13a that for the same r_o and v_g, D_{det} increases with an increase in σ. This is similar to the results of Ma et al. [11]. D_{det} becomes large because an increase in σ inhibits bubble detachment. The period of bubble generation becomes long (however, the frequency decreases). In particular, for the condition of a low v_g, D_{det} increases relatively significantly with an increase in σ; however, for the conditions of a large r_o and a high v_g, D_{det} varies slightly with an increase in σ. Jamialahmadi et al. [43] pointed out that bubble detachment volume is completely determined by the balance between buoyancy and surface tension at a low v_g, so σ is very important at a small v_g. However, as v_g increases, the effect of σ becomes less important.
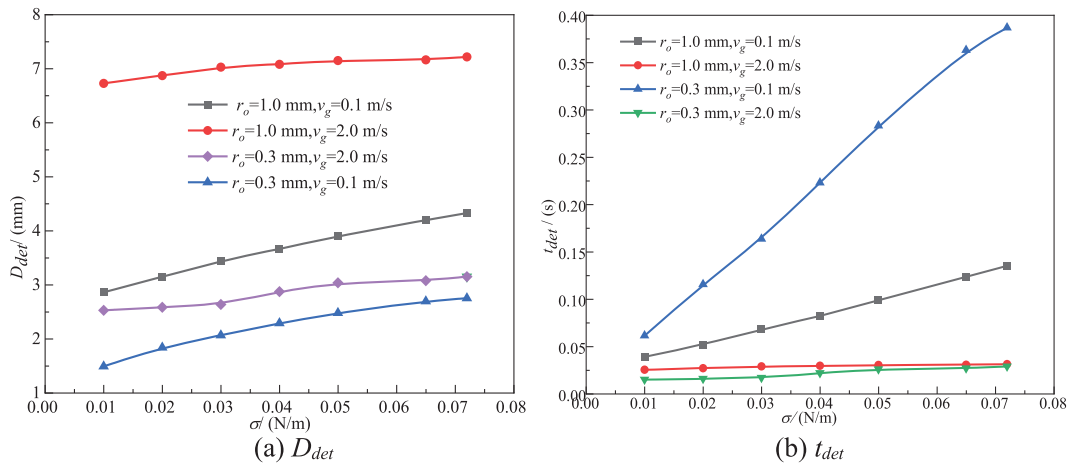

(a) D_{det} (b) t_{det}

Figure 13: Effect of σ on D_{det} and t_{det}

As shown in Fig. 13b, the effect of σ on t_{det} is related to r_o and v_g. When v_g is high ($v_g = 2.0$ m/s), t_{det} does not change much with an increase in σ for $r_o = 0.3$ and 1 mm. When v_g is small ($v_g = 0.1$ m/s), t_{det} increases with an increase in σ. And for a small r_o ($= 0.3$ mm), t_{det} increases greatly with an increase in σ; however, for a great r_o ($= 1.0$ mm), t_{det} increases slightly with an increase in σ. In short, σ is small, meaning that the force hindering bubble detachment becomes smaller. Therefore, t_{det} is short.

3.3.4 Liquid−Phase Viscosity

The effect of μ_l on D_{det} and t_{det} for the fixed r_o and v_g, and the basic parameters is shown in Fig. 14. It can be seen that D_{det} increases as μ_l increases. For a large r_o ($= 1$ mm) and a low v_g ($= 0.1$ m/s), D_{det} increases significantly with an increase in μ_l; however, for a small r_o ($= 0.3$ mm) and a low v_g ($= 0.1$ m/s), the change of D_{det} with an increase in μ_l is not very obvious. Moreover, the increase of D_{det} with an increase in v_g is not significant in the range of $\mu_l = 0.001$–0.1 Pa·s, and it is relatively obvious in the range of $\mu_l = 0.1$–0.5 Pa·s. A similar phenomenon is reported in reference [43]. When μ_l is high, the viscous drag is more important. Therefore, bubble detachment volume is greatly influenced by μ_l. When v_g is small, this effect is negligible.
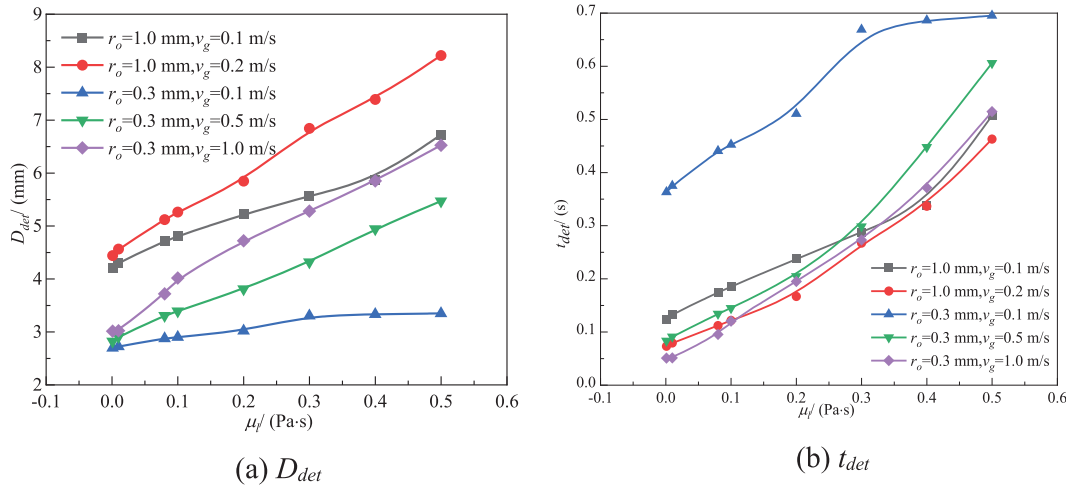

(a) D_{det}

(b) t_{det}

Figure 14: Effect of μ_l on D_{det} and t_{det}

When r_o is different, the trend of t_{det} changing with an increase in μ_l is also different. When $\mu_l \leq 0.3$ Pa·s, t_{det} increases slowly with an increase in μ_l. When $\mu_l > 0.3$ Pa·s, t_{det} increases quickly with an increase in μ_l except in the case of $r_o = 0.3$ mm and $v_g = 0.1$ m/s. For a small r_o ($= 0.3$ mm) and a low v_g ($= 0.1$ m/s), t_{det} increases dramatically first and then remains almost constant with an increase in μ_l. When r_o and v_g are small simultaneously, t_{det} will become very great.

3.3.5 Liquid−Phase Density

Fig. 15 shows the effect of ρ_l on D_{det} and t_{det} for the fixed r_o and v_g, and the basic parameters. It can be seen from Fig. 15a that D_{det} basically decreases as an increase in ρ_l. For the conditions of a large r_o ($= 1.0$ mm) and a large v_g ($= 1.0$ m/s), D_{det} decreases first and then remains almost constant as ρ_l increases. For the conditions of a large r_o ($= 1.0$ mm) and a low v_g ($= 0.1$ m/s), and a small r_o ($= 0.5$ mm), D_{det} decreases rapidly first and then slowly decreases with an increase in ρ_l. This verifies the results in Fig. 11.
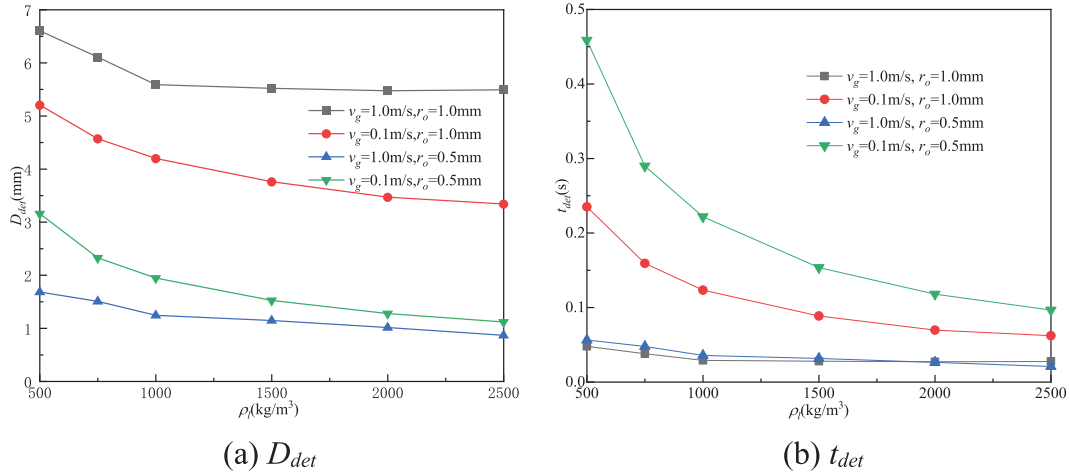
(a) D_{det} (b) t_{det}

Figure 15: Effect of ρ_l on D_{det} and t_{det}

It can be seen from Fig. 15b that the effect of ρ_l on t_{det} is related to r_o and v_g. t_{det} basically decreases with an increase in ρ_l. For a large r_o (= 1.0 mm) and a high v_g (= 1.0 m/s), t_{det} is almost constant with an increase in ρ_l. For a small r_o (= 0.5 mm) and a low v_g (= 0.1 m/s), t_{det} decreases substantially with increasing ρ_l. For the cases with a large (or small) r_o and a small (or large) v_g, t_{det} decreases slightly with an increase in ρ_l. When ρ_l is small, t_{det} is tightly related to r_o and v_g; however, when ρ_l is large, t_{det} is slightly influenced by r_o and v_g.

3.3.6 Comparative Analysis of Results

To quantitatively understand the effect of each parameter on D_{det} and t_{det}, the above results are comprehensively compared. It can be summarized as follows: (1) v_g increases by 60 times when increasing v_g from 0.05 to 3 m/s, which leads to an increase in D_{det} by 2 times and a decrease in t_{det} by 6.9 times. (2) r_o increases by 15 times when increasing r_o from 0.1 to 1.5 mm, causing an increase in D_{det} by 3 times and a decrease in t_{det} by 8.6 times. (3) a increases nearly by 3 times when increasing a from 3.71 to 10.99 m/s², causing an increase in D_{det} by 1.4 times and a decrease in t_{det} by 2.9 times. (4) σ increases by 7.2 times when increasing σ from 0.01 to 0.072 N/m, which leads to an increase in D_{det} by 1.5 times and a decrease in t_{det} by 3.46 times. (5) μ_l increases by 500 times when increasing μ_l from 0.001 to 0.5 Pa·s, which leads to an increase in D_{det} by 1.6 times and in t_{det} by 4.1 times. (6) ρ_l increases by 5 times when increasing ρ_l from 500 to 2500 kg/m³, causing an increase in D_{det} by 1.5 times and in t_{det} by 3.7 times. It can be found from the above results that μ_l has the least effect on D_{det} and t_{det}, and a has the greatest effect on D_{det} and t_{det}. Georgoulas et al. [15] also pointed out that a, σ, and ρ_l have significant effects on the detachment characteristics of bubbles (especially t_{det}), while the effect of μ_l is small.

4 Analyses of Bubble Generation Mechanisms

4.1 Force Model of Bubble Generation

The forces in the vertical direction during the bubble generation process are shown in Fig. 16. These forces can be divided into two main types. One is the forces that drive bubbles to detach, i.e., buoyancy force (F_B), pressure (F_P), and gas momentum force (F_M). The other is the forces that prevent bubbles from detaching, i.e., surface tension (F_S), viscous drag (F_D), and added mass force (F_{AM}).
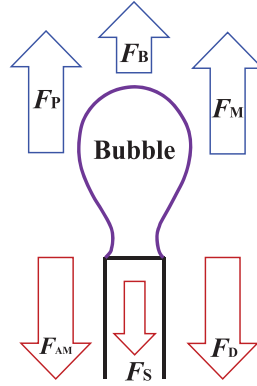
Figure 16: Forces in the vertical direction during bubble formation

The buoyancy force (F_B) is caused by the density difference between gas and liquid phases, and it is calculated by Eq. (10) [48].

$$F_B = g \left(\rho_l - \rho_g \right) V_b \tag{10}$$

where V_b denotes the instantaneous volume of the bubble, $V_b = \pi r_o^2 v_g t_{det}$; and t_{det} is bubble detachment time, s.

The pressure (F_P) is caused by the pressure difference between inside and outside a bubble, and the pressure at the bubble apex can be calculated by Eq. (11) [46].

$$F_P \approx \frac{2\pi r_o^2 \sigma}{r} \tag{11}$$

Here r is the instantaneous radius of the bubble, m.

The gas momentum force (F_M) is generated by the momentum of gas passing through the needle, and it can be calculated by Eq. (12) [8].

$$F_M = \frac{\rho_g}{\pi r_o^2} \left(\frac{dV_b}{dt} \right)^2 \tag{12}$$

The surface tension (F_S) is related to the contact perimeter and the contact angle (θ) between the bubble and the needle, and it can be calculated by Eq. (13) [23].

$$F_S = \frac{2\pi r_o^2 \sigma}{r} = 2\pi r_o \sigma \sin \theta \tag{13}$$

The added mass force (F_{AM}) is that during the bubble growth process, the accelerated motion of the bubble can drive the surrounding liquid to move together. It is the force that liquid prevents the change in the bubble interface. It can be calculated by Eq. (14) [49].

$$F_{AM} = \frac{d}{dt} \left[\left(\rho_g + \frac{11}{16} \rho_l \right) V_b \frac{dY_{CM}}{dt} \right] \tag{14}$$

where Y_{CM} is the axial centroid position of bubbles, m.

The viscous drag (F_D) before bubble separation is mainly determined by the growth rate of the center of mass in the vertical direction of the bubble and is calculated by Eq. (15) [50]:

$$F_D = \frac{1}{2}\pi\rho_L C_D r^2 \left(\frac{dY_{CM}}{dt}\right)^2 \tag{15}$$

where C_D is the drag coefficient, and it is a function of Reynolds number (Re), calculated by Eq. (16) [51].

$$C_D = \frac{15.34}{Re} + \frac{2.163}{Re^{0.6}} \tag{16}$$

Here $Re = 2\rho_l v_g r/\mu_l$ [8].

4.2 Flow Field Analyses of Bubble Generation Process

The flow field around bubbles, especially near the gas−liquid interface, helps to understand the role of the liquid phase during the formation of bubbles. Fig. 17 shows the flow field during the bubble generation process for some typical cases. The black line represents the bubble interface, the white arrows indicate the flow direction of fluids, and the background color indicates the magnitude of the local velocity of fluids. When gas is injected into liquid, as the bubble grows, the bubble volume increases and occupies the space previously occupied by the liquid, and the flow mode of the liquid changes due to the growth of the bubble. Due to the effect of surface tension, the gas−liquid interface is close to a sphere in shape. When the gas with a certain velocity enters the bubble, a circulation flow forms. Under the viscous effect, the liquid around the bubbles forms a circular flow too, due to the flow at the interface. At the later stage of bubble formation, the motion of the bubble interface pushes the liquid−phase motion in axial and radial directions, respectively. The liquid phase near the bubble interface has two velocity components. The radial component of velocity acting on the bubble interface is larger, and the bubble neck forms under its action. The smaller axial component of velocity can elongate the bubble along the axial direction so that the bubble interface evolves from a concave shape to a convex one. When the bubble neck moves along the axial direction, the liquid phase accelerates flow toward the bubble neck due to the conservation of mass. This prompts the bubble to further shrink at the bubble neck, resulting in the separation of the bubble. During bubble separation, there is a large gas velocity in the bubble neck, which leads to a drastic increase in the effect of gas inertia [13].

As shown in Fig. 17, on the basis of the basic parameter, the influence of v_g, μ_l, ρ_l, r_o, a, and σ on the flow field is analyzed. Comparing the flow field of $v_g = 0.1$ m/s with that of $v_g = 0.6$ m/s, it is found that at $v_g = 0.6$ m/s, the bubble growth simultaneously drives much more liquid around the bubble to move together due to the faster growth of the bubble (i.e., D_{det} is great and t_{det} is small), so the magnitude of velocity of the fluids around the bubble is large. At $v_g = 0.1$ m/s, the magnitude of liquid velocity is large only in a very narrow range at the top of the bubble. In addition, at $v_g = 0.6$ m/s, the circulation on both sides of the bubble is stronger at the same time (i.e., the velocity magnitude in the circulation zone is relatively large). This is very helpful for the formation of a bubble neck. The bubble is more easily elongated along the axial direction due to the large gas injection volume per unit time (i.e., a large gas momentum). So, at $v_g = 0.6$ m/s, D_{det} is relatively large, while t_{det} is relatively short.
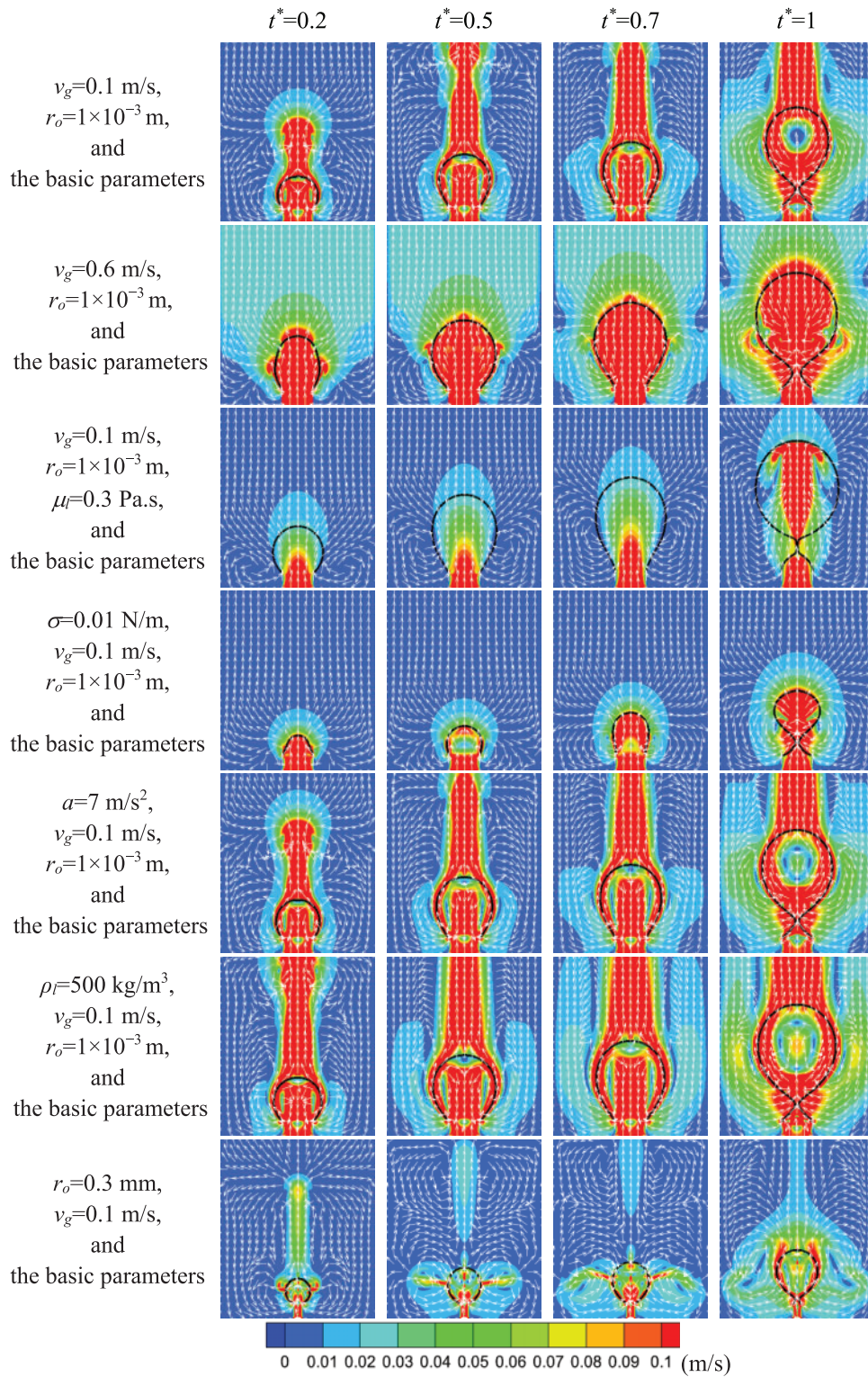
Figure 17: Flow field distribution during bubble generation process

Comparing the flow field of $\mu_l = 0.001$ with that of $\mu_l = 0.3$ Pa·s, it is found that at $\mu_l = 0.3$ Pa·s, the bubble growth is slower (i.e., t_{det} is longer and D_{det} is larger) because of the higher viscosity of the liquid (i.e., the viscous drag is great), and the magnitude of liquid velocity around the bubble is smaller. At $\mu_l = 0.3$ Pa·s, the circulation on both sides of the bubble weakens (i.e., the velocity magnitude in the circulation region becomes small) at the same time because of the higher viscosity of liquid. Thus, time is longer for the forces driving the separation of bubbles to increase enough to break the bubble neck. By comparing the flow fields of $\sigma = 0.065$ N/m with that of $\sigma = 0.01$ N/m, it is found that at $\sigma = 0.01$ N/m, t_{det} is short due to a decrease in σ, and thus the gas–liquid contact surface increases faster per unit time. Therefore, the influence range on liquid velocity around the bubble is small. Because t_{det} is small, the circulation on both sides of the bubble is close to the needle. This is very helpful to the generation of bubble neck.

As shown in Fig. 17, when $a = 7$ m/s^2 is relatively small, there is a small increase in the region of higher liquid velocity around the bubble because the liquid becomes lighter in weight, and the liquid around the bubble is more susceptible to bubble growth. The increase in the high–speed region of liquid leads to stronger circulation on both sides of the bubble (the velocity magnitude in the circulation region is relatively larger). This promotes the formation of a bubble neck. And at $a = 7$ m/s^2, t_{det} is relatively longer. Thus, the delayed detachment of the bubble leads to a larger D_{det}. This in turn leads to a decrease in surface tension (i.e., a decrease in the force hindering bubble detachment), and finally, the bubble detaches from the needle rim. The effect of ρ_l on the flow field is similar to that of a, and thus the related analyses are not repeated here.

When $r_o = 0.3$ mm is relatively small, the range of bubble growth affecting the surrounding liquid becomes narrow. This is caused by the fact that at the same v_g and t, the gas inflow becomes small for a small r_o. Thus, there is a decrease in bubble volume (i.e., a decrease in bubble interface) at the same time. Moreover, at $r_o = 0.3$ mm, the bubble is closer to a sphere in shape, meaning that the bubble grows at roughly the same speed in any radial direction, so the bubble growth has a significant effect on the radial and axial velocities of the surrounding liquid.

4.3 Pressure Field Analysis of Bubble Generation Process

The pressure contours corresponding to Fig. 17 are shown in Fig. 18, where the black line represents the bubble interface and the background color indicates the magnitude of the gas–liquid phase pressure. As shown in Fig. 18, the pressure inside the bubble (equal to the sum of the pressure generated by the surface tension and the hydrostatic pressure of liquid) is different from that of the surrounding liquid phase pressure since the bubble diameter during the formation process changes. The pressure is not uniform because the velocities of fluids inside and outside the bubble are different. Inside the bubble, the further away from the needle is, the smaller the gas velocity is; thus the closer to the bubble top is, the higher the pressure is. The pressure inside the bubble at the pre–growth stage ($t^* = 0.2$) is greater than that at the mid–growth stage ($t^* = 0.5, 0.7$), According to Eq. (11), the pressure inside the bubble becomes small with an increase in bubble diameter when other parameters remain unchanged. In the early and middle stages of bubble formation ($t^* = 0.2, 0.5,$ and 0.7), the total difference in the pressure between the bubble and liquid phases is large. As the bubble grows (bubble diameter becomes large), the pressure difference between the inside and outside of the bubble gradually decreases. At the late stage of bubble formation ($t^* = 1$), the gas–liquid pressure around the neck at the time of bubble detachment decreases. As mentioned in reference [14], when $\rho_l/\rho_g > 6.2$, the surface tension becomes very small and is negligible at the time of bubble detachment, and the bubble detachment is mainly caused by buoyancy. Gas flows through the bubble neck, and the gas velocity is very high. Then the pressure is low due to the Bernoulli effect (for an incompressible inviscid fluid at

a steady flow, when the pressure is low, the velocity is high in the same streamline). The suction force generated by the local low pressure affects both the gas and the surrounding liquid. The surrounding liquids are sucked towards the bubble neck, which strengthens the compression on the bubble neck.
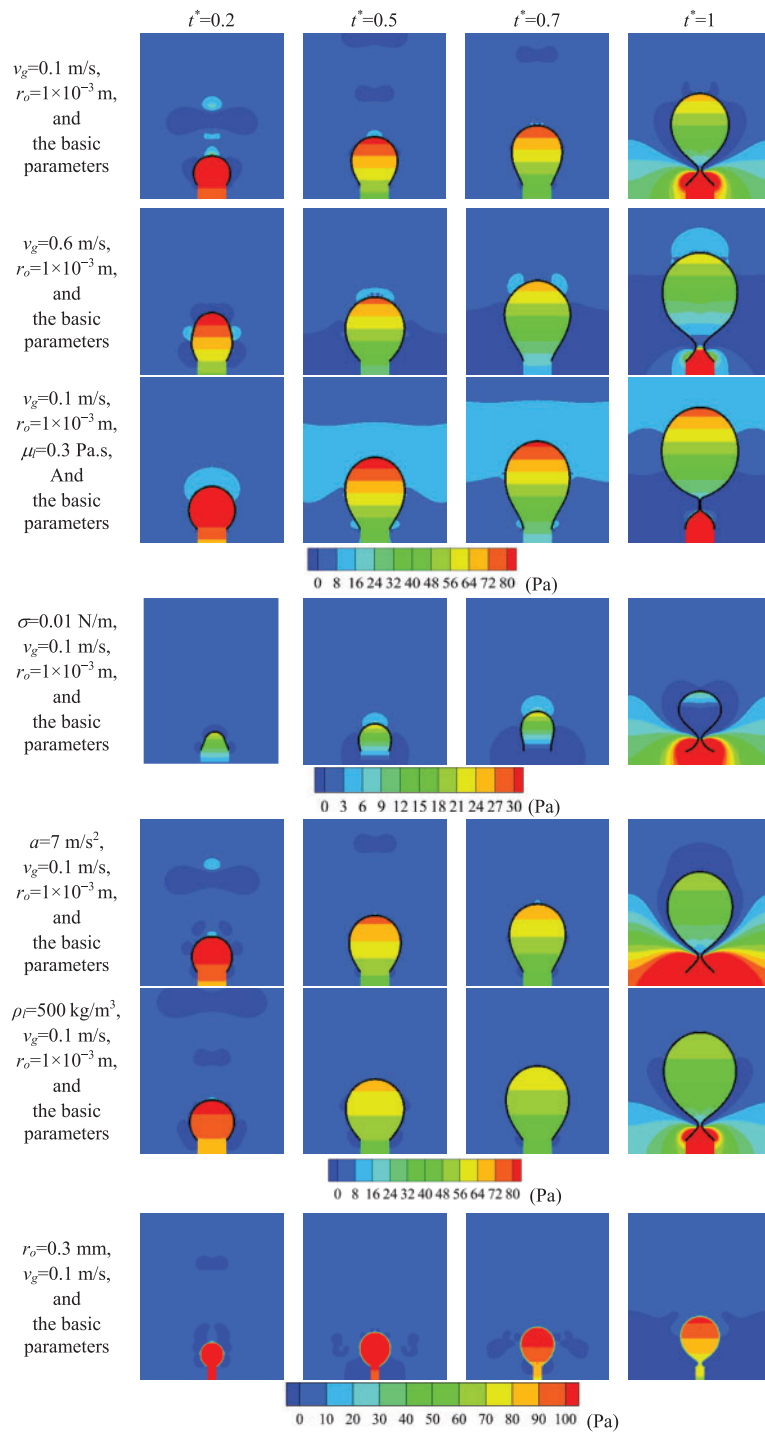

Figure 18: Pressure distribution during bubble generation process

As shown in Fig. 18, the bubble diameter is large at the same time at a large v_g compared with a small v_g, and therefore the pressure inside the bubble is relatively small. The pressure inside the bubble is relatively small at a large μ_l compared with a small μ_l. This is because a large μ_l leads to an increase in t_{det}, and the amount of gas entering the bubble is much more at a large μ_l. The pressure inside the bubble decreases significantly when σ decreases. This is consistent with Eq. (11). When a is relatively small, the pressure inside the bubble decreases. Since a decrease in a can lead to an increase in the bubble diameter at the same time. A decrease in ρ_l results in a decrease in the pressure inside the bubble. As shown in Fig. 15, t_{det} is almost independent of ρ_l at a small r_o. When the amount of gas entering the bubble remains constant, and the bubble volume is relatively large, the pressure inside the bubble is low. A decrease in r_o leads to the bubble radius is small. Therefore, the pressure inside the bubble increases substantially with an increase in r_o.

4.4 Force Analyses of Bubble Generation Process

To understand the bubble formation dynamics and the effect of each factor on bubble generation, the evolution of forces with time during bubble generation is analyzed. Fig. 19 shows the evolution of each force with time for $r_o = 1 \times 10^{-3}$ m, $v_g = 0.1$ m/s, and the basic parameters, where the resultant force is not equal to zero because the bubble is growing. At the early stage of bubble growth, the gas momentum is weak, buoyancy is very small, and the dominant forces are Fp and Fs. Fp, dependent on the pressure difference between the inside and outside of the bubble, is the maximum at the beginning of bubble growth. At this stage, the bubble shape is hemispherical, and the bubble diameter is very small. As the bubble diameter increases, Fp decreases monotonically with time. Fs is also related to needle radius and bubble diameter, so it also decreases with time. F_B is initially close to zero, and then it increases linearly as the bubble grows. The magnitude of F_M remains constant because v_g is uniform and relatively small. Thus, the growth rate of bubble volume is approximately constant. The viscous drag in low-viscosity liquids is negligible, so F_D is small and does not vary much. At the early and middle stages of bubble growth, because the bubble adheres to the needle rim, the axial center of mass position of the bubble changes slightly, and the additional mass force of the bubble hardly changes. With the formation of the bubble neck in the late stage, the additional mass force increases with an increase in the position of the center of mass. The resultant force is negative at the early stage of bubble growth, i.e., the direction of force is downward, at which the bubble adheres to the needle rim. At the middle and late stages of bubble growth, the magnitude of the resultant force changes from negative to positive, and it increases. Correspondingly, the bubble grows and is elongated along the axial direction, and it moves away from the needle until detaching. The present results are similar to those of references [4,29].

To understand deeply the effect of each factor on bubble generation, the effect of each factor on the main forces at the time of bubble separation is shown in Fig. 20. For the convenience of comparison, the absolute value of surface tension is adopted. It can be seen from Fig. 20a that the higher v_g is, the greater F_B is, and the smaller F_S and F_p are. The trend of F_S and F_p is similar. v_g increases, and accordingly, the bubble volume (diameter) increases. As shown in Eqs. (10) and (11), F_B becomes larger, but F_P becomes smaller. Surface tension is the dominant force at low flow rates; however, it has the minimum effect at high flow rates [46]. Therefore, F_S becomes smaller. As shown in Fig. 20b, with an increase in ρ_l, F_B decreases but F_S and F_p increase. Since an increase in ρ_l causes a corresponding increase in the density difference between the two phases, the bubble reaches a smaller volume. So, the buoyancy force decreases. As the effect of ρ_l on D_{det} is shown in Section 3, with an increase in ρ_l, D_{det} decreases. Therefore, F_S and F_p increase. It can be seen from Fig. 20c that as σ increases, F_B, F_S and F_p increase. As σ increases, F_S increases. The bubble volume is large enough (i.e., buoyancy is

great enough) to promote it to detach from the needle, so F_B increases. As shown in Eq. (11), F_p also increases. As shown in Fig. 20d, with an increase in μ_l, F_B increases but F_S and F_p decrease. This is because the greater the μ_l is, the greater the F_D is. This leads to a corresponding increase in buoyancy according to the force equilibrium. And bubble detachment volume is large at a high μ_l, so F_S and F_p decrease. It can be seen from Fig. 20e that F_B is almost unaffected by a, and F_S and F_p increase with an increase in a. This is because an increase in a leads to a decrease in D_{det} (as shown in Fig. 12), F_B changes insignificantly, while F_S and F_p increase. As shown in Fig. 20f, an increase in r_o causes an increase in F_B, F_S, and F_p. This is because surface tension is proportional to the orifice diameter [52]. The larger the needle size is, the greater the holding force is, and the bubble is attached to the orifice for a longer time. This causes a larger bubble volume (as shown in Fig. 11), and thus F_B increases. As shown in Eq. (13), F_p increases. F_p is weak for smaller orifices; however, it becomes predominant for larger orifices. So, F_p increases.
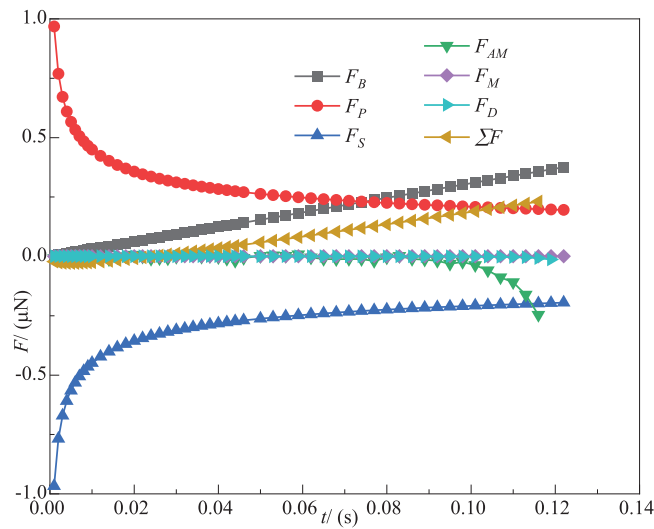

Figure 19: Variation of forces with time for $r_o = 1 \times 10^{-3}$ m, $v_g = 0.1$ m/s and the basic parameters
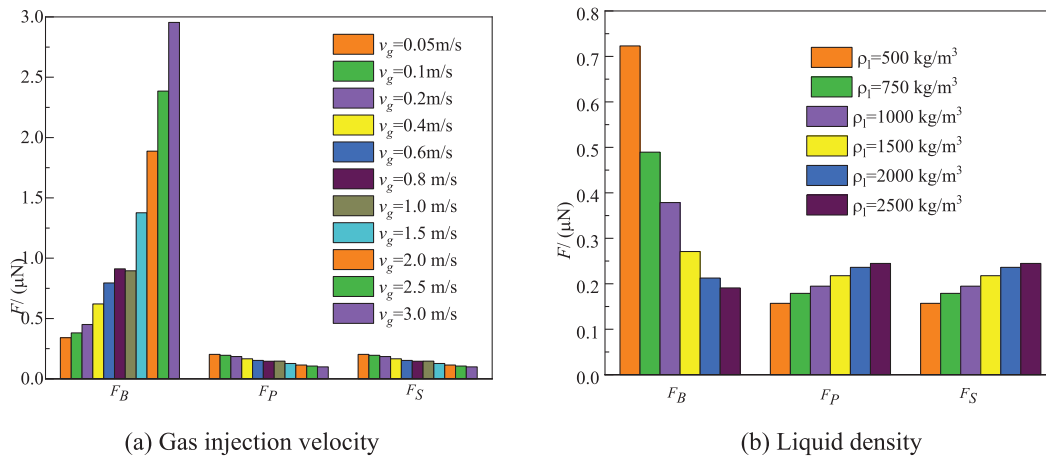

(a) Gas injection velocity

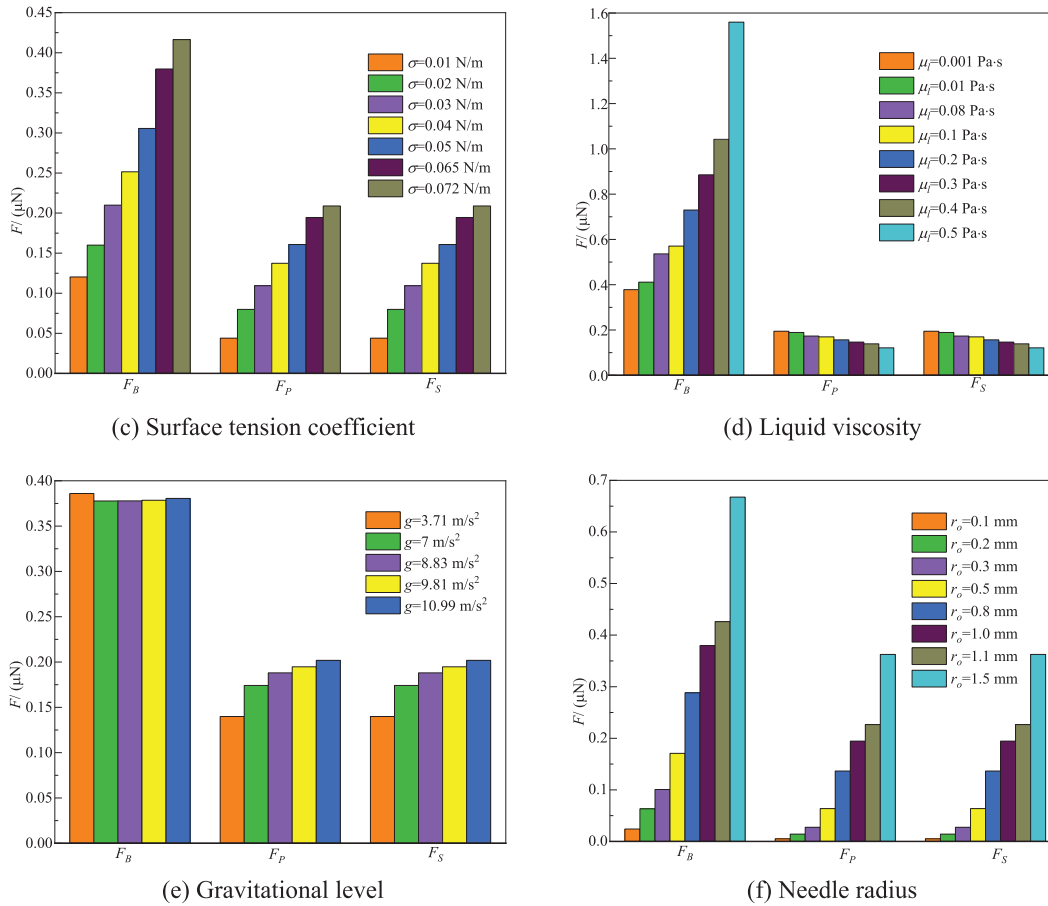(b) Liquid density

Figure 20: (Continued)

Figure 20: Analyses of forces on the bubble at the time of bubble separation

5 Conclusions

The effects of gas injection velocity, gravitational level, surface tension coefficient, liquid viscosity and density, and needle radius on bubble generation in Newtonian fluids are analyzed in detail using the VOF method, and the following conclusions can be obtained:

1. An increase in gas injection velocity, liquid phase viscosity, needle radius, and surface tension coefficient, and a decrease in liquid density and gravitational level generally leads to an increase in bubble detachment diameter. The effect of gas injection velocity on bubble shape is the greatest, and the effect of that on bubble detachment diameter can be neglected for a small needle radius. When both the needle radius and the gas inlet velocity are small, the effect of liquid viscosity on bubble detachment diameter is not obvious in the low viscosity range. When the gas injection velocity is large, the surface tension coefficient has almost no effect on bubble detachment diameter.

2. A decrease in needle radius, gravitational acceleration, and liquid density, as well as an increase in gas inlet velocity, surface tension coefficient, and liquid viscosity, generally leads to an increase in bubble detachment time. When the gas inlet velocity is large to a certain extent, the needle radius and the gas inlet velocity have almost no effect on the detachment time. When the needle radius and the gas inlet velocity are small, the detachment time does not vary with

liquid viscosity. When the needle radius and the gas inlet velocity are large, the liquid density has almost no effect on the detachment time. By analyzing the flow and pressure fields, it is found that an increase in gas injection velocity, needle radius, and surface tension coefficient, and a decrease in liquid phase viscosity, liquid density, and gravitational level lead to strong circulation on both sides of the bubble. An increase in surface tension coefficient, liquid phase viscosity, liquid density, and gravitational level, and a decrease in gas injection velocity and needle radius increase the pressure inside the bubble.

3. In contrast, the effect of liquid−phase viscosity on bubble detachment diameter and time is the least, and the effect of gravity level on them is the greatest. Other factors have a smaller effect on the detachment diameter but a greater effect on the detachment time.

4. By analyzing the forces during the bubble generation process, it is found that the bubble generation is mainly influenced by buoyancy, pressure, and surface tension. An increase in gas injection velocity, surface tension coefficient, and needle radius, as well as a decrease in liquid density and viscosity, leads to an increase in buoyancy. An increase in liquid density, surface tension coefficient, gravity level, and needle radius, as well as a decrease in liquid viscosity, and gas injection speed, leads to an increase in surface tension. An increase in liquid density, gravity level, needle radius, and gas injection velocity leads to a decrease in pressure. An increase in surface tension coefficient and liquid viscosity leads to an increase in pressure.

Author Contributions: The authors confirm their contribution to the paper as follows: study conception and design: Meng Jia, Mingjun Pang; data collection: Meng Jia; analysis and interpretation of results: Meng Jia, Mingjun Pang; draft manuscript preparation: Meng Jia. All authors reviewed the results and approved the final version of the manuscript.

Availability of Data and Materials: Not applicable.

Conflicts of Interest: The authors declare that they have no conflicts of interest to report regarding the present study.

References

1. Zhang, W., Wang, J., Su, Q., Li, B., Yu, K. et al. (2023). Polarization motion of bubbles in a non-uniform electric field. *Chemical Engineering Journal, 455,* 140767.
2. Sahasrabudhe, S. N., Chaudhari, S. S., Farkas, B. E. (2021). Experimental measurement of factors affecting dynamics of bubble growth from a submerged orifice: Applications to the frying process. *Journal of Food Engineering, 251,* 36–44.
3. Tamura, A., Katono, K. (2023). Investigation into hybridization of the two-fluid model and phase-field model for multi-scale two-phase flow simulations. *Journal of Nuclear Engineering and Radiation Science, 9(3),* 031404.
4. Kulkarni, A. A., Joshi, J. B. (2005). Bubble formation and bubble rise velocity in gas–liquid systems: A review. *Industrial & Engineering Chemistry Research, 44(16),* 5873–5931.
5. Wang, H., Yang, W., Yan, X., Wang, Y., Zhang, H. (2020). Regulation of bubble size in flotation: A review. *Journal of Environmental Chemical Engineering, 8(5),* 104070.

6. Suja, V. C., Rodríguez-Hakim, M., Tajuelo, J., Fuller, G. G. (2020). Single bubble and drop techniques for characterizing foams and emulsions. *Advances in Colloid and Interface Science, 286,* 102295.

7. Gardner, J. E., Wadsworth, F. B., Carley, T. L., Llewellin, E. W., Kusumaatmaja, H. (2023). Bubble formation in magma. *Annual Review of Earth and Planetary Sciences, 51(1),* 131–154.

8. Martín, M., Montes, F. J., Galán, M. A. (2006). Numerical calculation of shapes and detachment times of bubbles generated from a sieve plate. *Chemical Engineering Science, 61(2),* 363–369.

9. Quan, S., Hua, J. (2008). Numerical studies of bubble necking in viscous liquids. *Physical Review E, 77(6),* 066303.

10. Chakraborty, I., Biswas, G., Ghoshdastidar, P. S. (2011). Bubble generation in quiescent and co-flowing liquids. *International Journal of Heat and Mass Transfer, 54(21–22),* 4673–4688.

11. Ma, D., Liu, M., Zu, Y., Tang, C. (2012). Two-dimensional volume of fluid simulation studies on single bubble formation and dynamics in bubble columns. *Chemical Engineering Science, 72,* 61–77.

12. di Bari, S., Lakehal, D., Robinson, A. J. (2013). A numerical study of quasi-static gas injected bubble growth: Some aspects of gravity. *International Journal of Heat and Mass Transfer, 64,* 468–482.

13. Albadawi, A., Donoghue, D. B., Robinson, A. J. (2013). Influence of surface tension implementation in volume of fluid and coupled volume of fluid with level set methods for bubble growth and detachment. *International Journal of Multiphase Flow, 53,* 11–28.

14. Albadawi, A., Donoghue, D. B., Robinson, A. J. (2013). On the analysis of bubble growth and detachment at low capillary and bond numbers using volume of fluid and level set methods. *Chemical Engineering Science, 90,* 77–91.

15. Georgoulas, A., Koukouvinis, P., Gavaises, M., Marengo, M. (2015). Numerical investigation of quasi-static bubble growth and detachment from submerged orifices in isothermal liquid pools: The effect of varying fluid properties and gravity levels. *International Journal of Multiphase Flow, 74,* 59–78.

16. Simmons, J. A., Sprittles, J. E., Shikhmurzaev, Y. D. (2015). The formation of a bubble from a submerged orifice. *European Journal of Mechanics-B/Fluids, 53,* 24–36.

17. Hecht, K. J., Velagala, S., Easo, D. A., Saleem, M. A., Krause, U. (2019). Influence of wettability on bubble formation from submerged orifices. *Industrial & Engineering Chemistry Research, 59(9),* 4071–4078.

18. Ali, M. F., Yu, L., Chen, X., Yu, G., Abdeltawab, A. A. et al. (2019). Numerical modeling for characterization of CO_2 bubble formation through submerged orifice in ionic liquids. *Chemical Engineering Research and Design, 146,* 104–116.

19. Oshaghi, M. R., Afshin, H., Firoozabadi, B. (2019). Investigation of bubble formation and its detachment in shear-thinning liquids at low capillary and Bond numbers. *Theoretical and Computational Fluid Dynamics, 33,* 463–480.

20. Boubendir, L., Chikh, S., Tadrist, L. (2020). On the surface tension role in bubble growth and detachment in a micro-tube. *International Journal of Multiphase Flow, 124,* 103196.

21. Smith, W. R., Wang, Q. X. (2023). The role of surface tension on the growth of bubbles by rectified diffusion. *Ultrasonics Sonochemistry, 98,* 106473.

22. Burton, J. C., Waldrep, R., Taborek, P. (2005). Scaling and instabilities in bubble pinch-off. *Physical Review Letters, 94(18),* 184502.

23. Duhar, G., Colin, C. (2006). Dynamics of bubble growth and detachment in a viscous shear flow. *Physics of Fluids, 18(7),* 077101.

24. Taghi Esfidani, M., Reza, Oshaghi, M., Firoozabadi, B., Afshin, H. et al. (2017). Modeling and experimental investigation of bubble formation in shear-thinning liquids. *Journal of Fluids Engineering, 139(7),* 071302.

25. Hanafizadeh, P., Sattari, A., Hosseini-Doost, S. E., Nouri, A. G., Ashjaee, M. (2018). Effect of orifice shape on bubble formation mechanism. *Meccanica, 53,* 2461–2483.

26. Sun, Q., Gu, H., Yu, X., Yin, W. (2019). Bubble formation characteristic of submerged single-hole orifice in aerosol suspension. *Frontiers in Energy Research, 7,* 92.

27. Mohseni, E., Herrmann-Heber, R., Reinecke, S. F., Hampel, U. (2019). Bubble generation by micro-orifices with application on activated sludge wastewater treatment. *Chemical Engineering and Processing-Process Intensification, 143,* 107511.

28. Muilwijk, C., van den Akker, H. E. A. (2019). Experimental investigation on the bubble formation from needles with and without liquid co-flow. *Chemical Engineering Science, 202,* 318–335.

29. Sattari, A., Hanafizadeh, P. (2019). Bubble formation on submerged micrometer-sized nozzles in polymer solutions: An experimental investigation. *Colloids and Surfaces A: Physicochemical and Engineering Aspects, 564,* 10–22.

30. Mohseni, E., Kalayathine, J. J., Reinecke, S. F., Hampel, U. (2020). Dynamics of bubble formation at micro-orifices under constant gas flow conditions. *International Journal of Multiphase Flow, 132,* 103407.

31. Li, X., Su, W., Liu, Y., Yan, X., Wang, L. et al. (2021). Comparison of bubble velocity, size, and holdup distribution between single-and double-air inlet in jet microbubble generator. *Asia-Pacific Journal of Chemical Engineering, 16(2),* e2611.

32. Muilwijk, C., van den Akker, H. E. A. (2021). The effect of liquid co-flow on gas fractions, bubble velocities and chord lengths in bubbly flows. Part I: Uniform gas sparging and liquid co-flow. *International Journal of Multiphase Flow, 137,* 103498.

33. Muilwijk, C., van den Akker, H. E. A. (2021). The effect of liquid co-flow on gas fractions, bubble velocities and chord lengths in bubbly flows. Part II: Asymmetric flow configurations. *International Journal of Multiphase Flow, 138,* 103562.

34. Reuter, F., Ohl, C. D. (2021). Supersonic needle-jet generation with single cavitation bubbles. *Applied Physics Letters, 118(13),* 012043.

35. Garivalis, A. I., di Marco, P. (2022). Isolated bubbles growing and detaching within an electric field in microgravity. *Applied Thermal Engineering, 212,* 118538.

36. Sheng, L., Chang, Y., Deng, J., Luo, G. (2022). Mechanism and modeling of Taylor bubble generation in viscous liquids via the vertical squeezing route. *Chemical Engineering Science, 258,* 117763.

37. Rajesh, S., Peddada, S. S., Thiévenaz, V., Sauret, A. (2022). Pinch-off of bubbles in a polymer solution. *Journal of Non-Newtonian Fluid Mechanics, 310,* 104921.

38. Tanaka, K., Yamaguchi, T. (2022). Direct observation of bubble generation processes inside a molten pool during laser cladding. *Surface and Coatings Technology, 447,* 128831.

39. Shi, Q., Zhu, H., Zhu, J., Wu, N., He, H. et al. (2022). Effect of gas injection rate on bubble generation characteristics and coal flotation. *Fuel, 324,* 124744.

40. Sarkar, S., Sen, N., Singh, K. K. (2023). Bubble formation at top-submerged nozzles immersed in a quiescent liquid. *Progress in Nuclear Energy, 161,* 104709.

41. Qiu, H., Obata, K., Yuan, Z., Nishimoto, T., Lee, Y. et al. (2023). Quantitative description of bubble formation in response to electrolyte engineering. *Langmuir, 39(14),* 4993–5001.

42. Manthey, J., Guesmi, M., Schab, R., Unz, S., Beckmann, M. (2023). A sensitivity analysis on the bubble departure diameter for bubble growth due to oxygen super-saturation in highly purified water. *International Journal of Thermofluids, 18,* 100327.

43. Jamialahmadi, M., Zehtaban, M. R., Müller-Steinhagen, H., Sarrafi, A., Smith, A. M. (2001). Study of bubble formation under constant flow conditions. *Chemical Engineering Research and Design, 79(5),* 523–532.

44. López, J., Hernández, J., Gómez, P., Faura, F. (2004). A volume of fluid method based on multidimensional advection and spline interface reconstruction. *Journal of Computational Physics, 195(2),* 718–742.

45. Kasimsetty, S. K. (2008). *Theoretical modeling and correlational analysis of single bubble dynamics from submerged orifices in liquid pools*, vol. 108. USA: University of Cincinnati.

46. Bhunia, A., Pais, S. C., Kamotani, Y., Kim, I. H. (1998). Bubble formation in a coflow configuration in normal and reduced gravity. *AIChE Journal, 44(7),* 1499–1509.

47. Oguz, H. N., Prosperetti, A. (1993). Dynamics of bubble growth and detachment from a needle. *Journal of Fluid Mechanics, 257,* 111–145.

48. Terasaka, K., Tsuge, H. (1993). Bubble formation under constant-flow conditions. *Chemical Engineering Science, 48(19),* 3417–3422.

49. Li, H. Z., Mouline, Y., Midoux, N. (2002). Modelling the bubble formation dynamics in non-Newtonian fluids. *Chemical Engineering Science, 57(3),* 339–346.

50. Zhang, L., Shoji, M. (2001). Aperiodic bubble formation from a submerged orifice. *Chemical Engineering Science, 56(18),* 5371–5381.

51. Nahra, H. K., Kamotani, Y. (2003). Prediction of bubble diameter at detachment from a wall orifice in liquid cross-flow under reduced and normal gravity conditions. *Chemical Engineering Science, 58(1),* 55–69.

52. Davidson, L., Amick Jr, E. H. (1956). Formation of gas bubbles at horizontal orifices. *AIChE Journal, 2(3),* 337–342.